eprints@whiterose.ac.uk
https://eprints.whiterose.ac.uk/

Stepwise Magnetization Control Strategy for DC-Magnetized Memory Machine

Hui Yang, Shukang Lyu, Heyun Lin, *Senior Member, IEEE*, Z. Q. Zhu, *Fellow, IEEE*,
Fei Peng, Erxing Zhuang, Shuhua Fang and Yunkai Huang

Post Conference Paper

· *Abstract*—Memory machine (MM) equipped with hybrid permanent magnets (PMs), i.e., NdFeB and low coercive force (LCF) PMs, exhibits acceptable torque capability at low speeds and high efficiency at high speeds. Previous literatures have addressed that the constant power speed range (CPSR) of MMs can be further extended by online PM flux control, and the requirement of flux-weakening (FW) inverter current can be reduced as well. Nevertheless, how to coordinate the *d*-axis vector FW and PM magnetization control over a whole operating range in a reasonable manner remains unreported. Therefore, this paper proposes and implements a stepwise magnetization control strategy on a DC-magnetized memory machine based on the operating characteristics under various PM magnetization states and speed ranges. The configuration, principle and mathematical model of the investigated machine are introduced first. Then, the proposed control strategy is established by dividing the operating envelop into several FW regions, and an appropriate FW control scheme is utilized at each stage. It demonstrates that the CPSR can be effectively extended by simply applying the demagnetizing current pulses in several steps. This simplifies the control efforts considerably without resorting to continuous PM flux control and frequent actions of the switching devices. The effectiveness of the proposed control strategy is verified by experimental results.

Index Terms—Control strategy, DC-magnetized, flux weakening, memory machine, stepwise magnetization, variable flux.

NOMENCLATURE

k_{mr}	Magnetization ratio
B_{r1k}	Remanence flux density in kth recoil line
B_{r1}	Fully magnetized remanence of AlNiCo PM
B_{r2}	Remanence of NdFeB PM
$\psi_{a/b/c}$	Three-phase flux linkages
$i_{a/b/c}$	Three-phase currents
θ_e	Electrical angle of rotor position
ψ_{pm1}	Flux-linkages contributed by NdFeB PM
ψ_{pm2}	Flux-linkages contributed by AlNiCo PM
L_0	DC component of self-inductance
M_0	DC component of mutual-inductance
$L_{aa/bb/cc}$	Three-phase self-inductances
M_{ab}	Mutual inductance between phases A and B
M_{bc}	Mutual inductance between phases B and C
M_{ca}	Mutual inductance between phases C and A
$u_{d/q}$	d/q-axis voltages
$i_{d/q}$	d/q-axis currents
$L_{d/q}$	d/q-axis inductances
ω_e	Rotating angular speed
T_e	Electromagnetic torque
P	Pole-pair number
u_{smax}	Maximum inverter voltage
i_{smax}	Maximum inverter current
L_s	Winding inductance ($L_d=L_q=L_s$)
L_m	Fundamental magnitude of self-inductance
ω_{base}	Base speed
ω_{emax}	Maximum speed
$\omega_1 \sim \omega_4$	Transition speeds
ψ_{pmc}	Critical flux linkage at the transition point from flux-weakening region I to region II
$\Delta\psi_{pm}$	Flux linkage increment
ΔT	Number of MS manipulation steps
I_{demag}	Demagnetizing current pulse magnitude

H. Yang*, S. Lyu, H. Lin, F. Peng, E. Zhuang, S. Fang, and Y. Huang are with School of Electrical Engineering, Southeast University, Nanjing, China (e-mail: *huiyang@seu.edu.cn, phone: 025-8379-1815, seueelab_lsk@163.com, hyling@seu.edu.cn, seueelab_zex@163.com, pengfei@seu.edu.cn, shfang@seu.edu.cn, huangyk@seu.edu.cn).

Z.Q. Zhu is with Department of Electronic and Electrical Engineering, University of Sheffield, Sheffield, U.K. (z.q.zhu@sheffield.ac.uk).

I. INTRODUCTION

PERMANENT MAGNET (PM) MACHINES [1]-[4] are extensively employed for various applications due to high torque density and efficiency. To extend their constant power speed range (CPSR), the flux-weakening control is generally required due to the constant PM fields, which is widely recognized as a challenging issue for traction applications [2] [3]. Nowadays, various flux-weakening (FW) methods [4]-[43] are utilized to effectively expand the speed range of PM machines. Conventionally, the negative *d*-axis current and field current control strategies [4]-[10] can be employed to counteract the PM flux beyond the base speed. However, it is relatively electrically sophisticated due to the high dependence on the machine parameters and PI regulator, etc. Meanwhile, the continuous excitation copper loss is undesirable for high efficiency operation in FW region.

Memory machine (MM), as an alternative FW solution, was regarded as a promising candidate for wide-speed-range applications [11]-[43]. Since the magnetization state (MS) of the employed variable flux low coercive force (LCF) PMs can be varied by applying a temporary current pulse, the airgap magnetic fluxes can be flexibly regulated. Thus, the continuous *d*-axis FW current is reduced, and hence the associated excitation copper loss and iron loss particularly under high speed region are decreased significantly.

According to the magnetizing current pattern, MMs can be classified into AC- [11]-[31] and DC-magnetized [32]-[43] types. The AC-magnetized MMs can be designed as both a hybrid magnet configuration [12] and a pole-changing type [13]. The surface-mounted type hybrid magnet MM are designed by a simplified magnetic equivalent circuit method in [14]. In addition, AC-magnetized MMs normally adopt vector-control algorithm to apply a *d*-axis current pulse in stator windings to vary the magnetization level of LCF PMs [15]. S. Maekawa, etc. in TOSHIBA Corporation [16] proposed a two-step online magnetization method for fractional-slot MMs. It was reported that the two-step control is required to permit the magnetization of all LCF PMs. During the magnetization control, the *d*-axis current loop utilizes the inverse-model feedforward control, while the *q*-axis current loop employs feedback control [17]. In [18], three families of magnetizing trajectories can be identified, which is used to further extend the speed range, and the high efficiency control over an overall operating range can be achieved with a hysteresis controller for the MS operating algorithm. Besides, a flux-linkage observer based current decoupling method [19]-[20] was used to minimize the torque ripple during the magnetization transients. The MS manipulation can be implemented at zero speed, zero load condition by using voltage disturbance state filter to correct the estimates from a flux observer. The mismatch between simulated and measured operating efficiencies was highlighted and investigated in [20], and a hysteresis PI based method was employed to choose the magnetization timing over a duty-cycle operation to reduce the operational loss by accounting for the transient and steady-state energy consumption. The flux-concentrated MM designs are proposed [21]. The design suggestions are provided in [22] and [23] to reduce the magnetizing current and inverter rating. Besides, a method based on vector control is proposed for a spoke-type MM [24], and the operating envelop is analyzed in [25]. An existing drive is used to measure the *dq* inductances and torque characteristics of the machine at several MSs, including the cross-magnetization effects. An improved hybrid PM design is presented for MM, which employs Ferrite to stabilize the MS during the on-load operation [25]. The artificial neural network based MTPA control scheme for the spoke-type AC-magnetized MM is implemented to significantly simplify the control effort by reducing the effect of the inductance nonlinearity under different MSs [26]. Besides, a modified adaptive nonlinear filter (MANF) is proposed to achieve the magnetic flux linkage estimation and the online close-loop MS control [27]. In [28], an improved flux observer is proposed for the series hybrid-PM MM prototype to estimate the MS based on the structured neural network (SNN) instead of the conventional look-up table method. The SNN is utilized to describe the relationship between the inductance and current under different MS cases, resulting in a data filing space saving and an accurate PM flux linkage identification [29]. In [30], A closed loop method for magnetization manipulation that mitigates the effect of temperature is proposed.

For DC-magnetized MMs [32]-[43], the design procedure, modelling and control strategy for a doubly-salient MM (DSMM) are reported in [32]-[38], and the possibilities of dual-mode operation for the DSMM is investigated [35], i.e.,

the DSPM machine mode or the switched reluctance machine mode. Besides, a multimode optimization methodology for DSMM considering multiple operating conditions is proposed in [38]. The flux-modulated concept is extended to DC-magnetized MM to combine high torque density and wide flux regulation capability [39]. Very recently, various switched flux MMs (SFMMs) [40]-[43] were presented to resolve the demerits of relatively complicated decoupling current control in AC-magnetized ones, and large torque ripple issue in DSMMs.

The review of literatures shows that the control issues of AC-magnetized MMs have been already investigated, but a complete and workable global FW control strategy for DC-magnetized MMs is still unreported. In fact, differing from the conventional PM machines using only vector control for FW, the DC-magnetized MM requires a coordinated control scheme between the traditional *d*-axis current and the magnetization current pulse. Meanwhile, the related reports on how to deal with these two FW current components under different speed ranges in a reasonable manner are absent in the existing literatures. Hence, it is necessary to develop a new control strategy for effective speed extension and efficiency improvement over a wide operating range, which is the main focus of this paper.

In order to fill the abovementioned knowledge gap, this paper proposes a stepwise magnetization control strategy for DC-magnetized MM to extend its CPSR with a simplified control scheme and less FW currents injected by the inverter. The major contribution of this paper can be summarized as three aspects. 1) A new global FW control strategy is developed for the DC-magnetized MMs. 2) The mathematical models and operating characteristics under various PM magnetization states (MSs) and speed ranges are established and computed. Based on the operating characteristics in different speed ranges, an appropriate control method is developed at each stage. 3) A stepwise magnetization control strategy is proposed for DC-magnetized MMs. In the proposed control scheme, the operating regions are divided into different stages, the magnetization/demagnetization current pulses are energized only in several steps instead of a continuous MS manipulation control in the previous similar solutions. This new control scheme can avoid the frequent actions of the switching devices for energizing the magnetizing current pulse, and hence avoiding the complicated control efforts.

This paper is organized as follows: in Section II, the configuration and flux regulation principle of a proof-of-principle machine are described and addressed first, followed by the mathematical modelling. Afterwards, the proposed global control strategy is introduced in Section III based on different trajectories of the operating point movement along the current/voltage limit circles. The different FW regions will be numerically identified by calculating the transition speed. In FW region I, the synthetic conventional *d*-axis current and PM demagnetization FW based scheme is employed, while the *d*-axis current FW is simply employed in FW region II. In Section IV, a stepwise magnetization control strategy is proposed for the effective CPSR extension without complicated control effort. The Section V is devoted to the experimental verification of the proposed control strategy.

II. CONFIGURATION, OPERATING PRINCIPLE AND MATHEMATICAL MODEL OF INVESTIGATED MACHINE

A. Machine Configuration

In this paper, a three-phase, 12-stator-slot/14-rotor tooth SFMM [26] is used for verifying the feasibility of the developed control strategy. The machine configuration is illustrated in Fig. 1. The machine is mainly characterized by a doubly salient structure. Compared to the conventional switched flux PM machines, the SFMM employs a hybrid PM configuration. The additional diametrically magnetized AlNiCo PMs are embedded between the "U"-shape stator-tooth modules and the stator yokes, and the magnetizing coils are wound on the AlNiCo PMs. The NdFeB PM serves as the dominant contributor for air-gap flux density, while the LCF AlNiCo PM acts as the flux adjustor due to its changeable MS. Different from the conventional machines having PMs on the rotor, both the hybrid PMs and windings are located on the stator, which permits good armature reaction withstand capability and easy thermal dissipation. The salient rotor with neither magnets nor coils is similar to that of switched reluctance machines, which is mechanically robust.
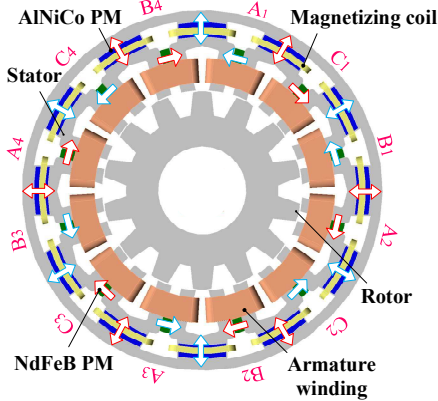

Fig. 1. Configuration of 12-stator-slot/14-rotor-tooth SFMM.

B. Flux Regulation Principle

The flux regulation principle of the proposed machine is illustrated by flux paths and open-circuit field distributions under different MSs as shown in Figs. 2 and 3. Firstly, when the rotor rotates, the alignment or misalignment between stator and rotor results in the variation of polarity and magnitude of PM fluxes interacting with the armature. Consequently, sinusoidal flux linkage will be induced. In addition, it is evident that the PM flux linkage can be flexibly varied since the MS of LCF PM can be adjusted with a magnetizing current pulse. Hence, the proposed SFMM can combine high torque density of conventional constant PM flux machine with variable PM flux characteristics for manipulating losses and high efficiency distributions within a duty-cycled operation. As a result, the NdFeB PMs serve as a dominant contributor for air-gap flux, while the LCF PMs work as a flux adjustor. The effective flux linked with the armature windings can be strengthened or weakened when the magnetization directions of LCF magnets are identical or opposite to those of NdFeB PMs, i.e., so-called the flux-enhanced and flux-weakened states, as illustrated in Fig. 3. Therefore, for low-speed region, NdFeB and LCF PMs are with identical magnetization direction, the torque density

can be subsequently improved. On the other hand, for high-speed region, the LCF PMs are reversely demagnetized to short-circuit and weaken the NdFeB PM fields, and hence the CPSR can be effectively extended within the limitation of the inverter power rating.
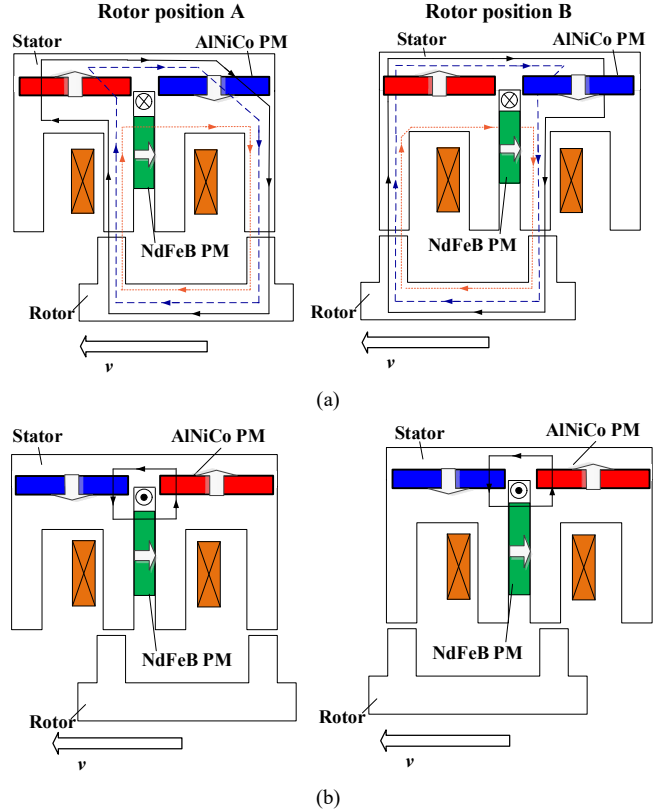

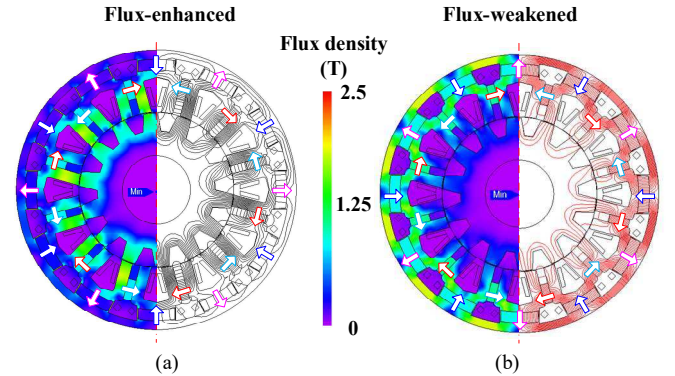Fig. 2. Operating principle of SFMMs. (a) Flux-enhanced. (b) Flux-weakened.

Fig. 3. The flux regulation principle of the SFMM denoted by the open-circuit field distributions. (a) Flux-enhanced. (b) Flux-weakened.
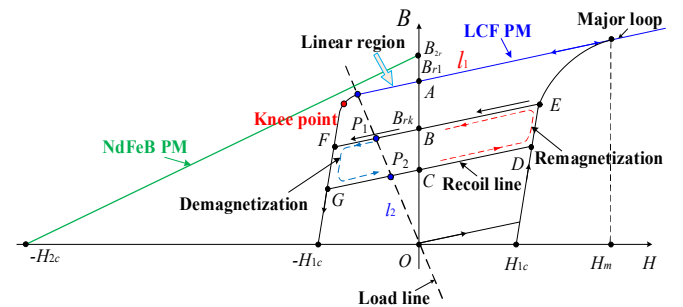

Fig. 4. Hysteresis curves of hybrid PM materials [32]-[40].

TABLE I
MAJOR DESIGN PARAMETERS OF 12-STATOR SLOT 14-ROTOR TOOTH SFMMS

Rated power (kW)	1.5
Rated speed (r/min)	1000
Rated current (Arms)	10
Full mag. current (A)	17.5
Stator outer radius (mm)	90
Stator inner radius (mm)	53.25
Air-gap length (mm)	0.5
NdFeB/AlNiCo Magnet grade	35SH/9DG
AlNiCo thick. (mm)	4
NdFeB thick. (mm)	2.5
AlNiCo length (mm)	10
NdFeB length (mm)	7.2
Active stack length (mm)	50
Stator tooth width (mm)	7.5
Rotor pole arc (deg.)	4.5
Turns of armature winding per phase	200
Turns of per magnetizing coil	80

The variable flux principle of the proposed DSPM-MM can be characterized by a simplified illustration of the parallelogram hysteresis model of LCF PMs as shown in Fig. 4 [32]-[40]. It can be seen that the coercive force of LCF PM is much lower than that of NdFeB. Thus, the PM working point can be repetitively shifted between different recoil lines by temporarily applying remagnetizing or demagnetizing current pulse. For instance, the working point of the PM is initiated at P_1, which is the cross point of the load line and the demagnetizing curve. When applying a demagnetizing current pulse, the working point will descend to G. After the withdrawal of the current pulse, the working point will move along a new recoil line and stabilize at new working point P_2. On the other hand, when a remagnetizing current pulse is applied, the working point of the PM will track the trajectory of $CDEB$ and return to P_1. Overall, the significant hysteresis nonlinearity in the second quadrant makes the operating points of LCF PM rather susceptible to the applied re-/de-magnetizing magneto-motive-force (MMF). Thus, the operating points can be shifted to a new recoil line by applying various magnitudes of current pulses.

A magnetization ratio k_{mr} is defined as the ratio of the remanence flux density corresponding to the kth recoil line B_{r1k} to the fully magnetized remanence B_{r1}, i.e.

$$k_{mr} = \frac{B_{r1k}}{B_{r1}}, \quad n = 1,2,3... \cdot \quad (1)$$

Here, the "flux-enhanced" and "flux-weakened" states refer to "$k_{mr}=1$" and "$k_{mr}=-1$", which indicate that the LCF PMs are fully magnetized in the same and opposite directions to the NdFeB PMs, respectively. Moreover, the "zero magnetized" state refers to the entire demagnetization of the LCF PMs, i.e., "$k_{mr}=0$". The key design parameters of the proposed machine are given in Table I.

C. Mathematical Model

1) Three-Phase Stationary Reference Coordinate

Different from the conventional switched flux PM machines [41], the flux linkage equations of the proposed SFMM include a changeable PM flux linage variable, which can be regarded as a nonlinear function of magnetizing or demagnetizing current magnitudes. This function can be obtained by either non-linear

finite element simulation or experiment. Hence, the flux linkage equations can be expressed as

$$\begin{bmatrix} \psi_a \\ \psi_b \\ \psi_c \end{bmatrix} = \begin{bmatrix} L_{aa} & M_{ab} & M_{ac} \\ M_{ba} & L_{bb} & M_{bc} \\ M_{ca} & M_{cb} & L_{cc} \end{bmatrix} \begin{bmatrix} i_a \\ i_b \\ i_c \end{bmatrix} + \begin{bmatrix} \cos(\theta_e) \\ \cos(\theta_e+120°) \\ \cos(\theta_e-120°) \end{bmatrix} (\psi_{pm1} + k_{mr}\psi_{pm2}) \quad (2)$$

The inductance matrix in (2) can be represented as

$$\begin{cases} L_{aa} = L_0 - L_m \cos(2\theta_e) \\ L_{bb} = L_0 - L_m \cos(2\theta_e+120°) \\ L_{cc} = L_0 - L_m \cos(2\theta_e-120°) \end{cases} \quad (3)$$

$$\begin{cases} M_{ab} = M_{ba} = M_0 - M_m \cos(2\theta_e - 120°) \\ M_{bc} = M_{cb} = M_0 - M_m \cos(2\theta_e) \\ M_{ca} = M_{ac} = M_0 - M_m \cos(2\theta_e + 120°) \end{cases} \quad (4)$$

The relationships between L_0, M_0, L_m, and M_m can be represented as

$$\begin{cases} L_0 = -2M_0 \\ L_m = M_m \end{cases} \quad (5)$$

2) dq-Axis Rotating Reference Coordinate

The voltage equations can be given based on the rotor reference frame without considering magnetic saturation, iron loss and temperature dependences, i.e.

$$\begin{cases} u_d = R_s i_d + L_d \dfrac{di_d}{dt} - \omega_e L_q i_q \\ u_q = R_s i_q + L_q \dfrac{di_q}{dt} + \omega_e (L_d i_d + \psi_{pm1} + k_{mr}\psi_{pm2}) \\ T_e = \dfrac{3}{2} P \left[i_q (\psi_{pm1} + k_{mr}\psi_{pm2}) + i_d i_q (L_d - L_q) \right] \end{cases} \quad (6)$$

where u_d and u_q are the d/q-axis voltages, i_d and i_q are the d/q-axis currents, L_d and L_q are the d/q-axis inductances; R_s is the stator winding resistance. ω_e is the rotating angular speed; T_e is the electromagnetic torque; P is the pole-pair number, i.e., the rotor tooth number. Due to unity saliency ratio ($L_d \approx L_q$), the torque output can be readily controlled by the armature and magnetizing currents, as reflected in the third equation of (6).

III. DESCRIPTION OF THE GLOBAL CONTROL STRATEGY

The proposed global control strategy combines the distinct advantages of memorable flux and negative d-axis current FW controls, leading to an effective extension of CPSR with improved efficiency as well as low requirement of inverter current.

A. Overall Control Diagram

For the constant-torque region, the control method for the investigated SFMM is similar to that for the conventional sinusoidal-fed PM machines [30]. Due to the unity saliency ratio, the $I_d=0$ control is utilized for MTPA control. On the other hand, the conventional negative I_d FW and PM demagnetization controls are combined in constant power region. The overall block diagram of the proposed control strategy is shown in Fig. 5. The control circuit mainly includes two modules, i.e., drive and FW control modules, and the former is based on a space vector pulse width modulation (SVPWM), and the latter adopts a negative feedback control. The core part of the magnetization control circuit is a single-phase H bridge converter similar to the PWM chopper

[37]. The amplitude of the current pulse can be regulated by the means of single current closed-loop control.

The optimal coordinated FW control scheme for the conventional d-axis current FW and magnetization controls will be analyzed in the following context to extend CSPR based on the detailed analysis on the trajectory of operating point movement along the current/voltage limit circles.
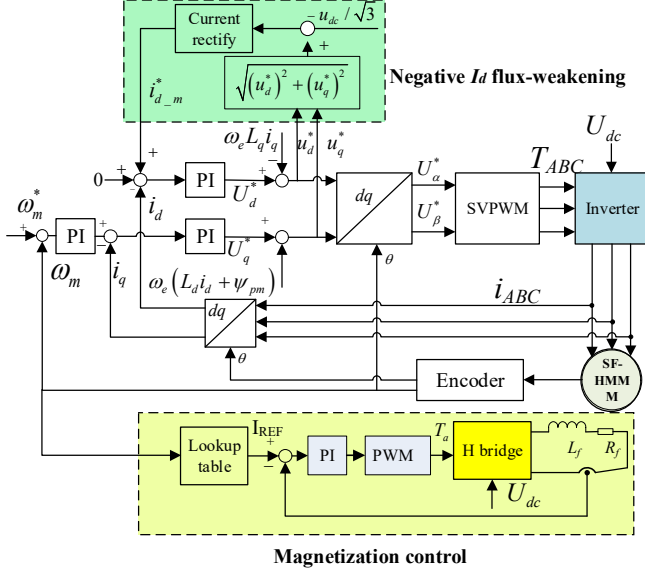

Fig. 5. Overall block diagram of the proposed global control strategy.

B. Voltage/Current Limit Circles

The operating points of the machine are constrained by the maximum inverter voltage and current (u_{smax} and i_{smax}), which can be expressed as

$$\left| \boldsymbol{u}_s \right| = \sqrt{u_d^2 + u_q^2} \le \left| \boldsymbol{u}_{s\max} \right| \quad (7)$$

$$i_d^2 + i_q^2 \le i_{s\max}^2 \quad (8)$$

Under the high-speed operation, the resistance drop can be ignored, and hence (7) can be rewritten in terms of d- and q-axis voltages:

$$\left| \boldsymbol{u}_s \right| = \sqrt{\left(\omega_e \left(\psi_{pm1} + k_{mr} \psi_{pm2} \right) + \omega_e L_s i_d \right)^2 + \left(\omega_e L_s i_q \right)^2} \le \left| \boldsymbol{u}_{s\max} \right| (9)$$

i.e.

$$L_d^2 \left(i_d + \frac{\psi_{pm1} + k_{mr} \psi_{pm2}}{L_d} \right)^2 + \left(L_q i_q \right)^2 \le \frac{\left| \boldsymbol{u}_s \right|_{\max}^2}{\left(\omega_e \right)^2} \quad (10)$$

Since the d and q-axis inductances are very close to those of SFMM, (8) can be rewritten in terms of the d- and q-axis currents

$$\left(i_d + \frac{\psi_{pm1} + k_{mr} \psi_{pm2}}{L_s} \right)^2 + \left(i_q \right)^2 \le \frac{\left| \boldsymbol{u}_s \right|_{\max}^2}{\left(L_s \omega_e \right)^2} \quad (11)$$

From the assumption of unity saliency for the SFMMs, $L_d = L_q = L_s$ (the winding inductance). It can be seen that the d- and q-axis voltages are mutually coupled. Consequently, the third terms of the first two equations in (6) can be utilized as a disturbance value for the feedforward so as to eliminate the voltage cross-coupling. According to the constraint functions in (10) and (11), the current/voltage limit circles can be illustrated in Fig. 6, which are used as a basis for the next investigation.

As the machine speed increases, the radius of the voltage limit circle decreases inversely proportionally as indicated in (10). On the other hand, for a given speed, when LCF PMs are demagnetized, i.e., k_{mr} decreases, the center of the voltage limit circle shifts towards point O in Fig. 6(a). The FW current I_d will exceed the characteristic current (the ratio of the flux linkage to d-axis inductance) as long as the center of voltage limit circle locates inside the current limit circle. Meanwhile, the machine speed can be theoretically infinite, as illustrated in Fig. 6(b). This also theoretically confirms the feasibility of PM demagnetization control for effective speed range extension.

C. Operating Characteristics Analysis under Different Speed Regions

The proposed global control strategy divides the operating region into three sub-regions as shown in Fig. 7, which refer to constant-torque region, FW I and FW II regions, respectively. The division of the operating regions is based on the movement of operating points along the voltage/current circles, as addressed later. Under the constant-torque region, zero d-axis current control is employed, when $i_q = i_{smax}$ (inverter maximum current), the machine reaches to the base speed (ω_{base}), which can be expressed as

$$\omega_{base} = \frac{\left| \boldsymbol{u}_s \right|_{\max}}{\sqrt{\left(\psi_{pm1} + k_{mr} \psi_{pm2} \right)^2 + \left(L_s i_{s\max} \right)^2}} \quad (12)$$

At this time, the corresponding operating trajectory refers to "OA" in Fig. 8. When the rotation speed continues to rise, the machine will subsequently entry the FW region, which can be subdivided into two sub-regions based on the relationship between i_{smax} and $(\psi_{pm1} + k_{mr} \psi_{pm2})/L_s$.

1) FW Region I: $(\psi_{pm1} + k_{mr} \psi_{pm2})/L_s > i_{smax}$

In FW region I, when the machine speed increases, the operating point will gradually reach the critical position so as to maintain the sufficient torque output. Then, the torque will drop to zero when the current and voltage circles are just tangent, i.e., the machine speed reaches the maximum (ω_{emax}), which can be represented as

$$\omega_{e\max} = \frac{\left| \boldsymbol{u}_s \right|_{\max}}{L_s i_d + \psi_{pm1} + k_{mr} \psi_{pm2}} \quad (13)$$

The corresponding trajectory of operating point refers to "AB" in Fig. 9(a).
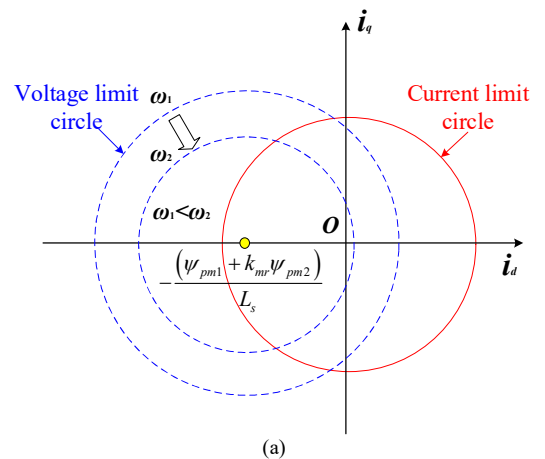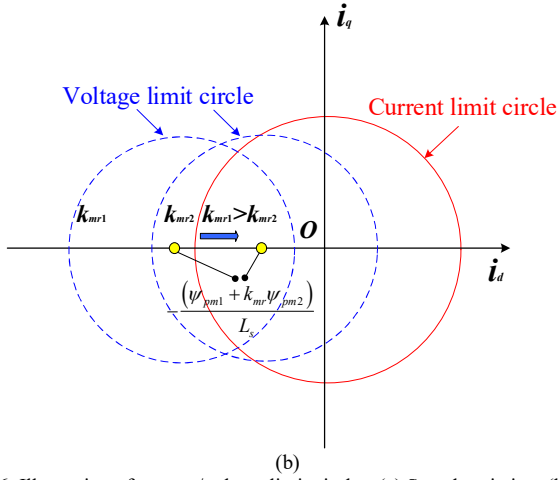

(a)

Fig. 6. Illustration of current/voltage limit circles. (a) Speed variation. (b) Flux linkage variation.

2) FW Region II: $(\psi_{pm1}+k_{mr}\psi_{pm2})/L_s{\leq}i_{smax}$

In FW region II, as the flux-linkage is reduced to a certain value with the aid of the demagnetization control, the working point $(-(\psi_{pm1}+k_{mr}\psi_{pm2})/L_s, 0)$ locates inside the current circle, the operating speed range is theoretically infinite. This deep FW region can be further subdivided into two stages.

a) Stage 1:

Similar to in FW region I, the radius of current circle proceeds to decrease with increasing machine speed in this stage. The operating speed will shift to the perpendicular line across point C for maintaining sufficient torque output. During this process, the operating point tracks along the MTPA trajectory. The maximum achievable speed can be expressed as

$$\omega_{e\max} = \frac{|u_s|_{\max}}{\sqrt{(L_s i_{s\max})^2 - (\psi_{pm1} + k_{mr}\psi_{pm2})^2}} \quad (14)$$

b) Stage 2:

In this stage the operating point for the maximum torque will move along line BC, i.e., maximum torque per voltage (MTPV) line, and the corresponding maximum speed can be expressed as

$$\omega_{e\max} = \frac{|u_s|_{\max}}{L_s i_q} \quad (15)$$

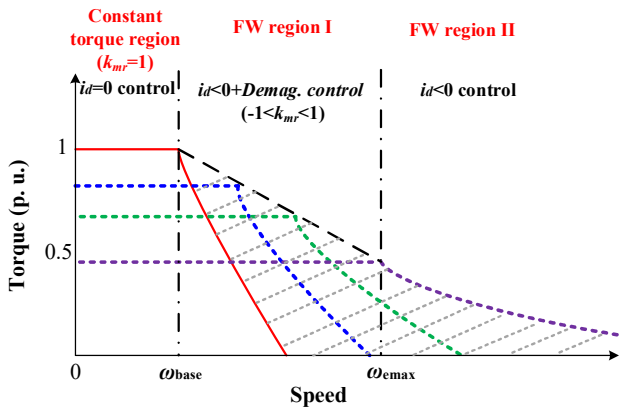The operating trajectory refers to "BC" (ω) in Fig. 9(b).

Fig. 7. Illustration of global control strategy by integrating PM magnetization

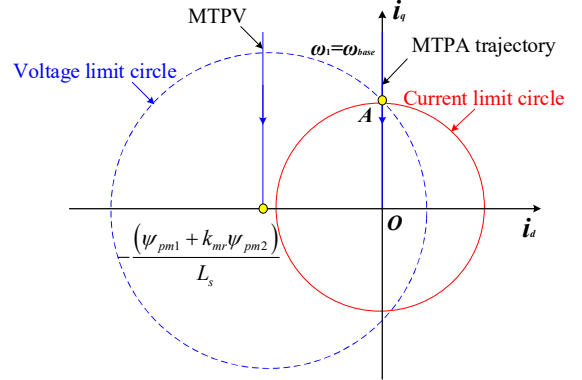and d-axis current flux weakening controls.

Fig. 8. Constant torque region illustrated by current/voltage limit circles.

IV. STEPWISE MAGNETIZATION CONTROL FOR EFFECTIVE SPEED RANGE EXTENSION

According to the preceding analyses, the torque-speed curves corresponding to different operating regions are plotted in Fig. 10. It can be observed that the demagnetization control can be performed first at point A in Fig. 9(a), i.e., the PM flux-linkage will be reduced so as to increase the base speed. On the other hand, when the machine entries FW region II, the resultant flux-linkage is unable to offer sufficient torque output, and consequently the demagnetization for AlNiCo PMs is no longer necessary, as indicated in Fig. 10(b).

The optimal operating characteristics can be synthesized as a set of continuous torque speed curves under different MSs of LCF PMs as shown in Fig. 11(a). The memorable flux and conventional d-axis current based FW controls can be combined at different speed regions to obtain CPSR as wide as possible. Fig. 11(b) shows the resultant optimal torque-speed curve by only choosing five typical MSs of LCF PMs, which is very close to the torque-speed curve shown in Fig. 11(a). That is to say, the flux memorable control can be implemented in several steps at the speeds from ω_1 to ω_4 to achieve a wide CPSR similar to the continuous magnetization control. Thus, the proposed stepwise magnetization control strategy can effectively avoid complicated continuous demagnetization control that is adverse to the dynamic performance boost. Meanwhile, the transient power loss of the switchers can be also significantly reduced.
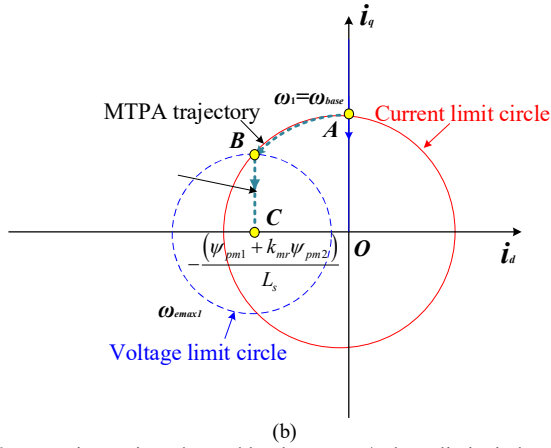

(a)

(b)
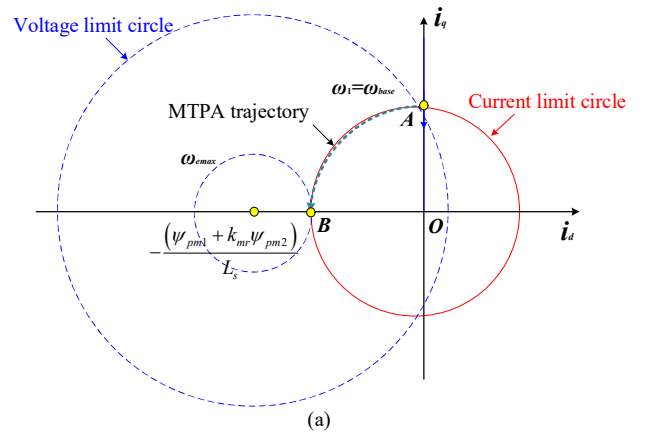
Fig. 9. Operating regions denoted by the current/voltage limit circles. (a) FW mode I. (b) FW II.

The purpose for the selection criterion of the magnetization states (MSs) is to simplify the online magnetization control by choosing proper steps of magnetization manipulation. If the steps are excessive, the frequent actions of the switching devices make the online MS control relatively complicated, while the speed extension tends to be less effective when few steps are chosen for MS manipulation. In this case, five typical operating curves are selected, and the resultant overall operating envelop turns out to be close to that with continuous MS control.

The calculation process of those transition speeds ω_1-ω_4 of the selected operating curves can be organized as follows. First of all, various torque versus speed curves under several MSs can be obtained. Then, the critical flux linkage Ψ_{pmc} corresponding to the transition point from flux-weakening region I to region II can be calculated by

$$\psi_{pmc} = \psi_{pm1} + k_{mr}\psi_{pm2} = L_s I_{s\max} \qquad (16)$$

Consequently, the flux linkage increment $\triangle\psi_{pm}$ for dividing the MS control steps can be obtained as

$$\triangle\psi_{pm} = \frac{\psi_{pm1} + \psi_{pm2} - \psi_{pmc}}{\triangle T} \qquad (17)$$

where $\triangle T$ denotes the number of MS manipulation steps. Thus, the typical flux linkages and torque-speed curves under five typical MSs can be obtained. As a result, the transition speeds ω_1-ω_4 can be calculated using the intersection points of the selected torque-speed curves.
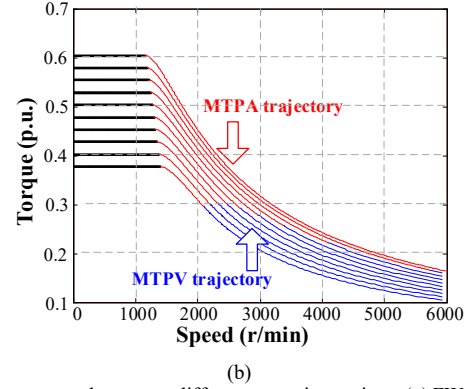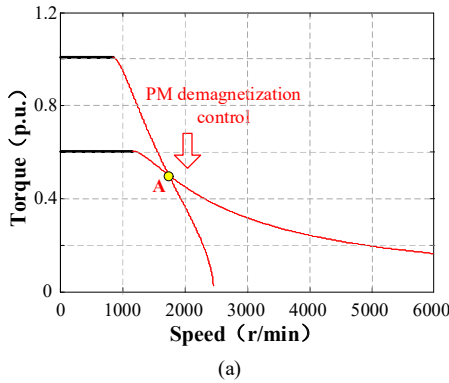

(a)

(b)

Fig. 10. Torque-speed curves at different operating regions. (a) FW region I. (b) FW region II.
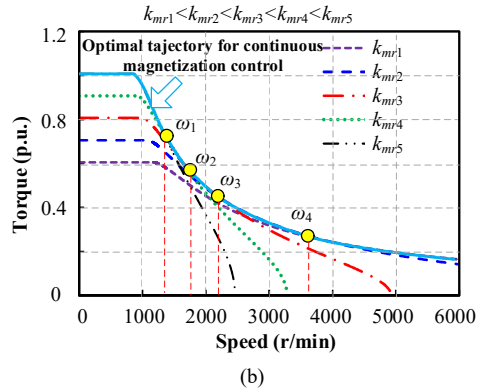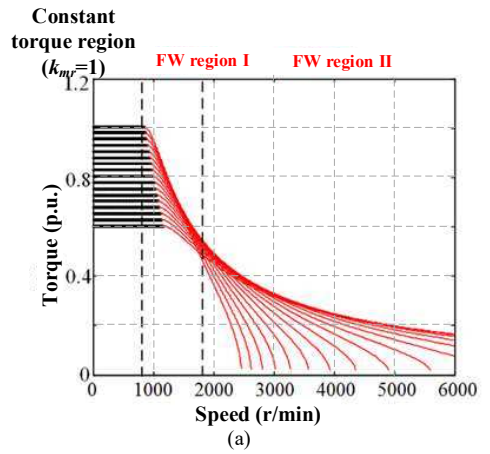

(a)

(b)

Fig. 11. Optimal operating envelops with (a) Continuous demagnetization, and (b) Stepwise demagnetization control strategy.

I. EXPERIMENTAL VALIDATION

In order to verify the effectiveness of the developed control strategy, a DSP-TMS320F28335 based experimental platform is constructed, and the manufactured SFMM prototype and control board are shown in Fig. 12. The ONOSOKKI TS-7700 Torque Station is utilized to generate a load torque.

The finite element (FE) predicted and measured back-EMF waveforms of the prototype machine under different MSs are shown in Fig. 13(a). It can be observed that the measured results agree well with the FE predictions. The fact that the manufacturing tolerance and end-effect ignorance are ignored in FE analyses is mainly responsible for the slight mismatch

between FE and measured results. Fig. 13(b) shows the variations of FE predicted- and measured- RMS back-EMFs with the current pulse amplitude, which confirms the excellent flux regulation capability of the proposed machine.

The on-load transient magnetization performance has been tested. The responses of phase current, speed and d/q-axis currents versus magnetizing current pulses are shown in Figs. 14 and 15, respectively. For the demagnetization situation, the machine starts with a given speed of 900r/min. Subsequently, a demagnetizing current pulse of -12A is applied to weaken the air-gap flux. It can be seen that the phase current amplitude swiftly rises up to 12.5A, due to the constant load with speed closed-loop control, as well as the flux-weakening action. For the demagnetization case under the constant-torque region (I_d=0 control) as shown Fig. 15(a), the machine starts with a given speed of 900r/min. Subsequently, the speed of SFMM fluctuates during the demagnetization and remagnetization process. However, it returns to the reference speed within a very short time, and then remains stable. As shown in Fig. 15(b), due to the constant load with speed closed-loop control as well as the flux-weakening action, the phase current sharply varies with the magnetizing state of PMs.
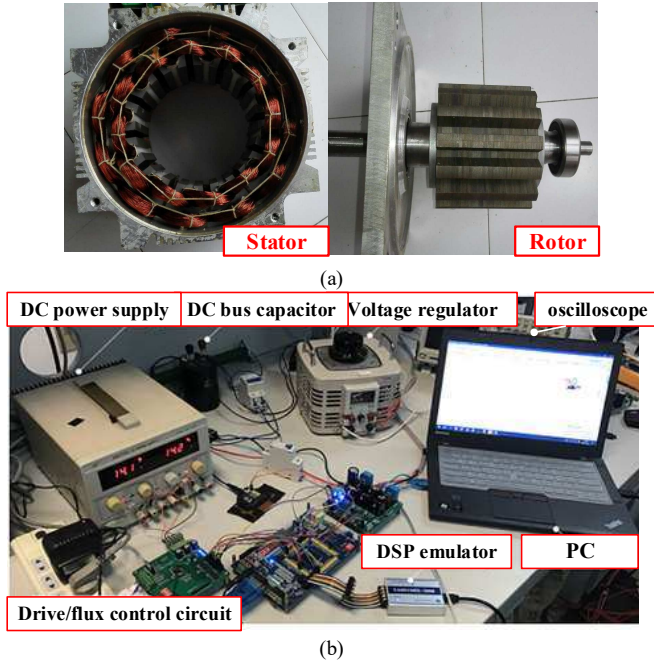

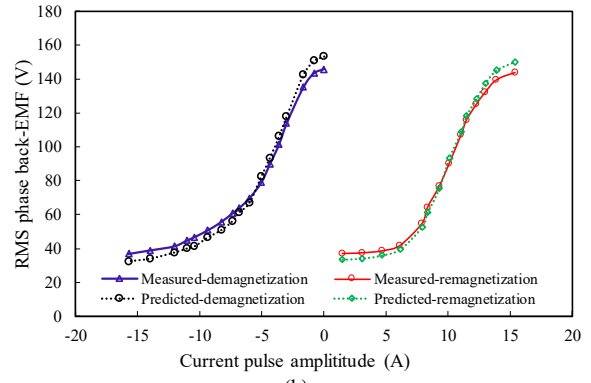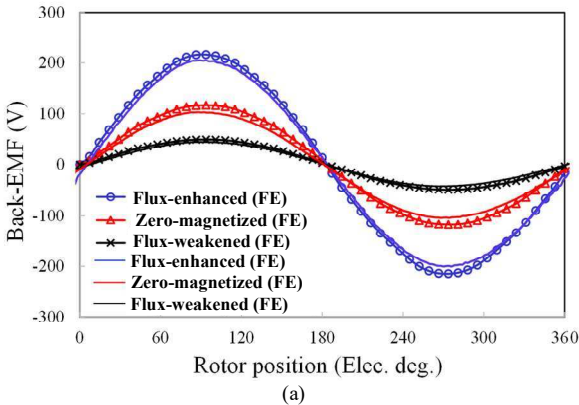Fig. 12. Experimental setup. (a) The prototype SFMM. (b) Control board.

Fig. 13. Comparison of FE-predicted and measured back-EMFs under different magnetization states. (a) Waveforms. (b) EMFs versus current pulse amplitudes.
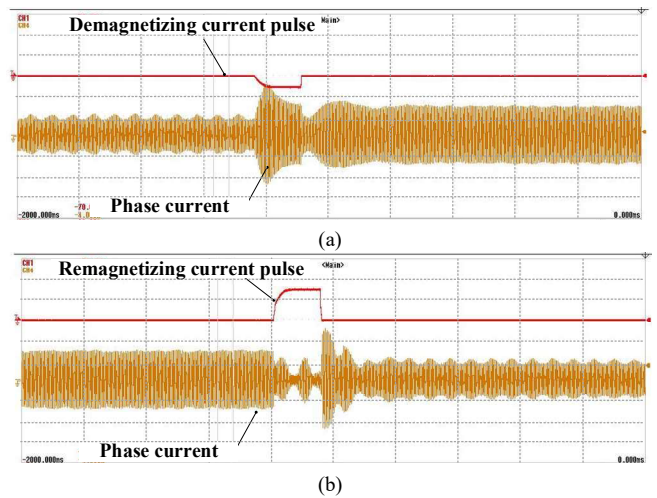

Fig. 14. Measured on-load transient responses of phase current to (a) remagnetizing current pulse and (b) demagnetizing current pulse, current pulse (20A/div.); current (10A/div.); time (200ms/div).
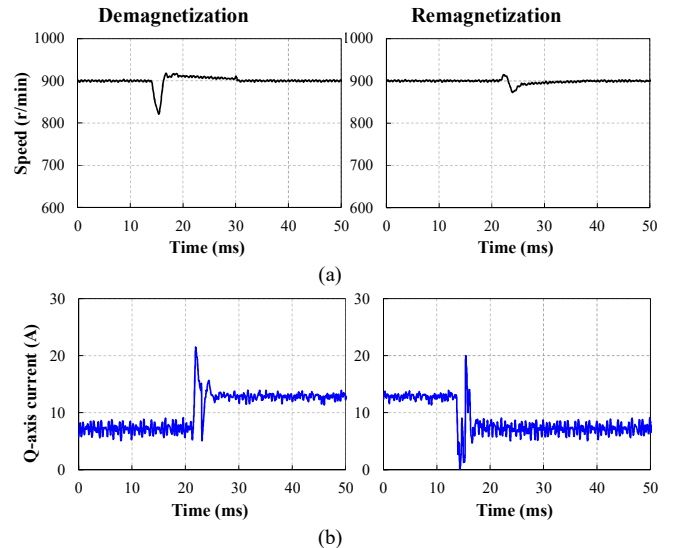

Fig. 15. Measured on-load demagnetization performance of the prototype SFMM in the constant-torque region. (a) Speed. (b) Q-axis current.

The working principle of a DC current pulse generator is shown in Fig. 16, which is utilized to illustrate the

magnetization process based on the proposed control strategy. Through the MS selector, the target MS can be obtained according to the operating speeds of the SFMM. The relationship between the current pulse magnitude and PM flux linkage during the demagnetizing and remagnetizing processes will be stored in the two look-up tables. The comparison between the target PM flux linkage and the present PM flux linkage will decide whether to demagnetize the PMs or remagnetize the PMs. Through the output of the look-up tables and the comparator, the current pulse to change the MS of PMs can be finally generated. With the proposed control strategy, the synthetic torque/power-speed curves can be obtained and the operating region of the SFMM is extended.

The measured torque/power-speed curves of the machine with or without the proposed control strategy are shown in Fig. 17, where I_{demag} is the demagnetizing current magnitude. The transition points where the temporary PM demagnetization controls are applied for different operation regions have been highlighted to reveal the merit of the proposed control scheme.
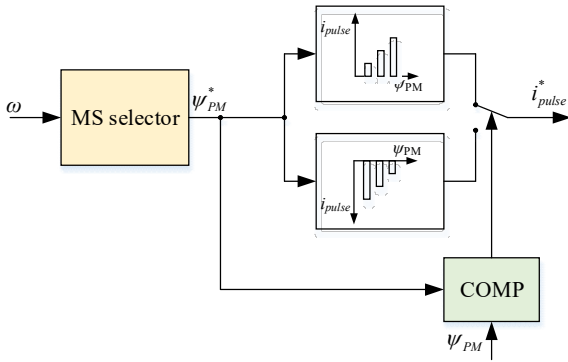

Fig. 16. Diagram of the magnetizing current pulse generator.

The torque-speed curve labelled with "without the proposed control" refers to the case with "$k_{mr}=1$" and only conventional d-axis current based FW control. On the other hand, the PM demagnetization and conventional d-axis current based FW controls are combined at different speed regions to extend the CPSR as wide as possible. As a result, with the proposed control strategy, a new torque-speed curve synthesized by choosing different MS (labelled with different "I_{demag}") is obtained. It shows that the proposed control strategy with stepwise performing online PM demagnetization control can effectively extend the CPSR compared to the case with only traditional d-axis FW current control. In fact, the measured results indicates that the machine can further extend the adjustable speed range beyond 5000 r/min, as reflected in the power/speed curves in Fig. 17(b). The critical flux linkage in the transition point from FW region I to region II can be estimated based on equation (1) as abovementioned. Consequently, the required demagnetizing current pulse can be further calculated based on Fig. 13. It implies that when the PM flux linkage is reduced to 58.6% of that at the flux-enhanced state, the negative d-axis current FW control rather than the combined control method can be simply employed for the CPSR extension. Overall, the measured results validate the preceding analyses, i.e., the flux-weakening capability can be effectively improved with the proposed control strategy. Fig.

18 shows the measured efficiencies of the machine at different speeds, respectively.
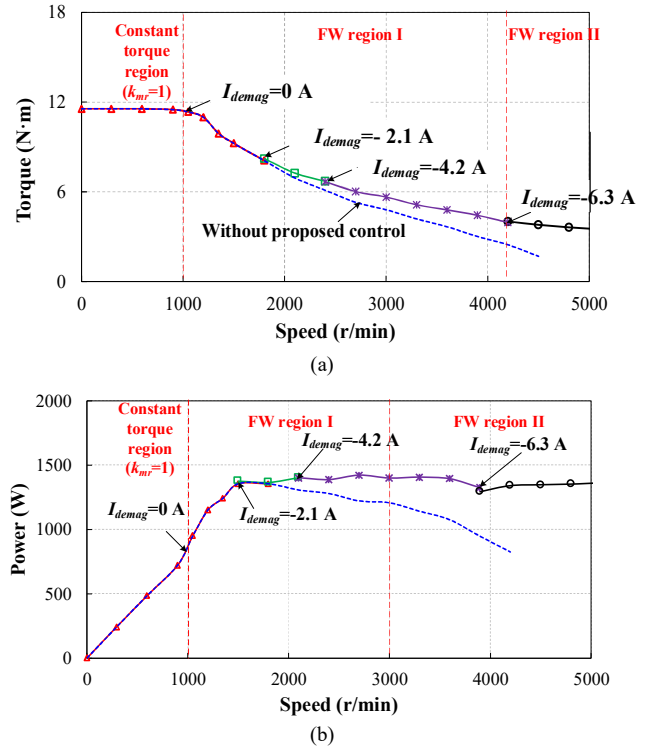

(a)

(b)

Fig. 17. Measured torque/power speed curves of the prototype machine with or without the proposed control strategy. (a) Torque-speed. (b) Power-speed.

In order to illustrate the magnetization process under the proposed control strategy when the machine entries the FW operation region, Fig. 18 shows the transient characteristics of the transition point ($I_{demag}= - 4.2A$) between two adjacent operating regions under different MSs including demagnetizing current pulse, d-axis current, q-axis current, speed and phase current. As shown in Fig. 18(a), a demagnetizing current pulse with the magnitude of - 4.2A and 20ms-duration is injected to demagnetize the AlNiCo magnets of the SFMM. Due to the reduction of PM flux linkage, the magnitude of d-axis FW current is decreased while the magnitude of q-axis current is increased, which are shown in Figs. 18(b) and (c). In addition, the demagnetizing current pulse leads to the drop of electromagnetic torque, and hence a q-axis current pulse in Fig 18(c) is produced to compensate the torque drop. The fluctuation of speed is shown in Fig. 18(d), which is inconspicuous, but the dynamic response is relatively slow due to the large load moment of inertia of the magnetic powder brake in the ONOSOKKI TS-7700 Torque Station. In Fig 18(e), the phase current amplitude of the SFMM is reduced after the change of PM flux-linkages. That is to say, the associated copper loss is also reduced with the proposed control strategy at the transition point which has the same speed and load.
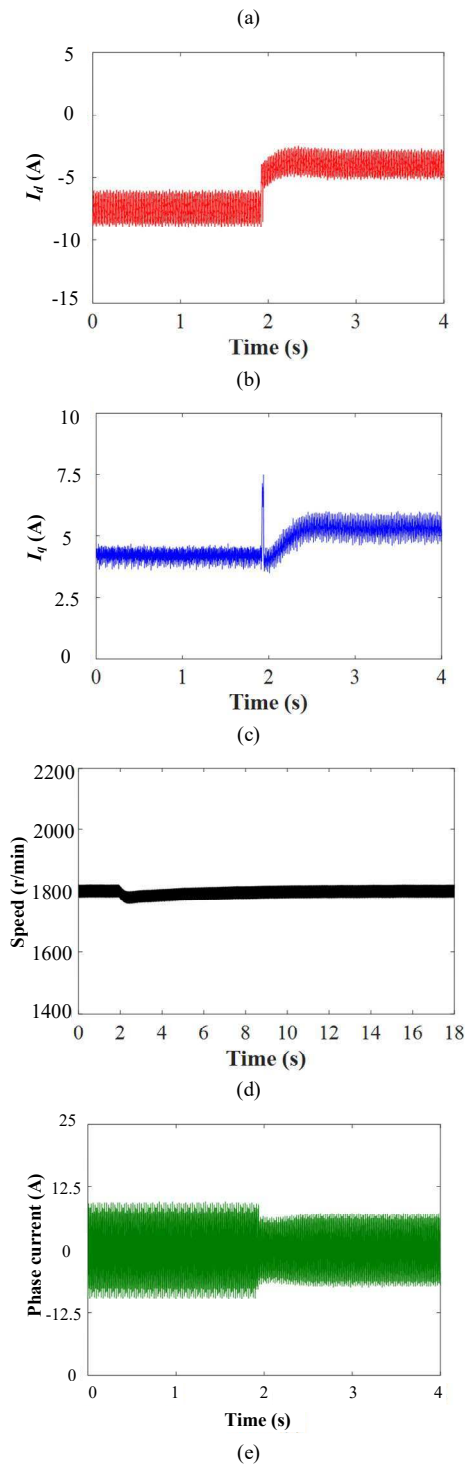
(a)

(b)

(c)

(d)

(e)
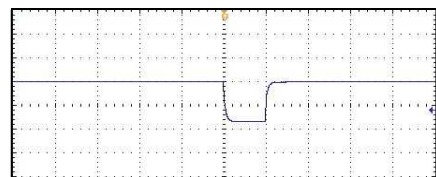
Fig. 18. Measured transient magnetization progress corresponding to one of the transition points in the optimal torque-speed curve under the FW region. (a) Demagnetizing current pulse (20ms/div, 2.5A/div). (b) d-axis, and (c) q-axis current characteristics. (c) Speed. (e) Phase current.

Fig. 19 shows the measured efficiencies of the machine at different speeds, respectively. The efficiency is measured using the output mechanical power divided by the input electrical power. The output mechanical power is calculated by multiplying the output torque and speed measured by the torque meter. Besides, the input electrical power is measured by a power analyzer (Yokogawa WT1800 precision). It can be seen

that when the proposed control strategy is employed, higher efficiency at high speeds can be achieved. This confirms the benefit of the developed control scheme in terms of the efficiency improvement over a wide speed range.
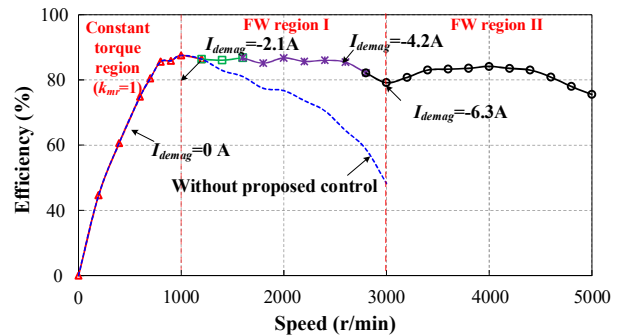

Fig. 19. Measured efficiency against speed curves with or without the proposed stepwise magnetization control strategy.

II. CONCLUSIONS

This paper proposes a stepwise magnetization control strategy for SFMM to avoid the complicated control efforts with the continuous and frequent adjustment of the PM flux linkage with the current pulse. The proposed control strategy is established by dividing the overall operating envelop into several regions based on the operating characteristics under various PM MSs. For FW region I, the negative I_d and the demagnetization current should be combined to extend the speed range, while the demagnetization control becomes useless during the deep FW region II. Furthermore, it shows that the resultant optimal torque-speed curve by only choosing five typical MSs of LCF PMs is very close to that obtained by the continuous magnetization control. That is to say, the proposed control scheme can effectively extend the CPSR as wide as the continuous control method with sophisticated magnetization manipulation. Finally, the effectiveness of the proposed control strategy is verified by experimental results.

REFERENCES

[1] G. A. Capolino and A. Cavagnino, "New trends in electrical machines technology," *IEEE Trans. Ind. Electron.*, vol. 61, no. 8, pp. 4281–4285, Aug. 2014.

[2] Z. Q. Zhu, "Permanent magnet machines for traction applications," in *Encyclopedia of Automotive Engineering,* John Wiley & Sons, Ltd., 2014.

[3] K. T. Chau, C. C. Chan, and C. Liu, "Overview of permanent-magnet brushless drives for electric and hybrid electric vehicles," *IEEE Trans. Ind. Electron.*, vol. 55, no. 6, pp. 2246-2257, May 2008.

[4] M. Ehsani, K. M. Rahman, and H. A. Toliyat, "Propulsion system design of electric and hybrid vehicles," *IEEE Trans. Ind. Electron.*, vol. 44, no. 1, pp. 19–27, Feb. 1997.

[5] C. Jo, J. Y. Seol, and I. J. Ha, "Flux-weakening control of IPM motors with significant effect of magnetic saturation and stator resistance," *IEEE Trans. Ind. Electron.*, vol. 55, no. 3, pp. 1330–1340, Mar. 2008.

[6] W. L. Soong and N. Ertugrul, "Field-weakening performance of interior permanent-magnet motors," *IEEE Trans. Ind. Appl.*, 2002, vol. 38, no. 5, pp. 1251-1258, Nov. 2002.

[7] S. Morimoto, M. Sanada, and Y. Takeda, "Wide-speed operation of interior permanent magnet synchronous motors with high-performance current regulator," *IEEE Trans. Ind. Appl.*, vol. 30, no. 4, pp. 920–926, Jul./Aug. 1994.

[8] H. Liu, Z. Q. Zhu, E. Mohamed, Y. Fu, and X. Liu, "Flux-weakening control of nonsalient pole PMSM having large winding inductance, accounting for resistive voltage drop and inverter nonlinearties," *IEEE Trans. Power Electron.*, vol. 27, no. 2, pp. 942-952, Feb. 2012.

[9] Tursini M, Chiricozzi E, and Petrella R, "Feedforward flux-weakening control of surface-mounted permanent-magnet synchronous motors accounting for resistive voltage drop," *IEEE Trans. Ind. Electron.*, vol. 57, no. 1, pp. 440-448, Jan. 2010.

[10] G. Borocci, F. G. Capponi, G. De Donato and F. Caricchi, "Closed-loop flux-weakening control of hybrid-excitation synchronous machine drives," *IEEE Trans. Ind. Appl.*, vol. 53, no. 2, pp. 1116-1126, Mar./Apr. 2017.

[11] V. Ostovic, "Memory motors," *IEEE Ind. Appl. Mag.*, vol. 9, no. 1, pp. 52-61, Jan./Feb. 2003.

[12] K. Sakai, K. Yuki, Y. Hashiba, N. Takahashi, and K. Yasui, "Principle of the variable-magnetic-force memory motor," in *Proc. Int. Conf. Electr. Mach. Syst.*, Tokyo, Japan, 2009, pp. 1-6.

[13] Y. Nariaki, and K. Sakai, "A permanent magnet motor capable of pole changing for variable speed drive," in *Proc. Int. Conf. Elect. Mach. Syst. (ICEMS)*, Busan, 2013, pp. 1127-1132.

[14] J. Y. Song, J. H. Lee, D. W. Kim, Y. J. Kim and S. Y. Jung, "Analysis and modeling of permanent magnet variable flux memory motors using magnetic equivalent circuit method," I*EEE Trans. Magn.*, vol. 53, no. 11, pp. 1-5, Nov. 2017.

[15] T. Kato, N. Limsuwan, C. Y. Yu, K. Akatsu, and R. D. Lorenz, "Rare earth reduction using a novel variable magnetomotive force flux-intensified IPM machine," *IEEE Trans. Ind. Appl.*, vol. 50, no. 3, pp. 1748-1756, May 2014

[16] S. Maekawa, K. Yuki, M. Matsushita, I. Nitta, Y. Hasegawa, T. Shiga, T. Hosoito, K. Nagai, and H. Kubota, "Study of the magnetization method suitable for fractional-slot concentrated-winding variable magnetomotive-force memory motor," *IEEE Trans. Power Electron.*, vol. 29, no. 9, pp. 4877-4887, Sep. 2014.

[17] C. Y. Yu, T. Fukushige, N. Limsuwan, T. Kato, D. D. Reigosa, and R. D. Lorenz, "Variable-flux machine torque estimation and pulsating torque mitigation during magnetization state manipulation," *IEEE Trans. Ind. Appl.*, vol. 50, no. 5, pp. 3414-3422, Sep. 2014.

[18] B. S. Gagas, K. Sasaki, T. Fukushige, A. Athavale, T. Kato, and R. D. Lorenz, "Analysis of magnetizing trajectories for variable flux PM synchronous machines considering voltage, high-speed capability, torque ripple, and time duration," *IEEE Trans. Ind. Appl.*, vol. 52, no. 5, pp. 4029-4038, Jun. 2016.

[19] B. Gagas, T. Fukushige, T. Kato, and R. D. Lorenz, "Operating within dynamic voltage limits during magnetization state increases in variable flux pm synchronous machines," in *Proc. IEEE Energy Convers. Congr. Expo.*, Sep. 2014, pp. 5206–5213.

[20] T. Fukushige, N. limsuwan, T. Kato, K. Akatsu, and R. D. Lorenz, "Efficiency contours and loss minimization over a driving cycle of a variable flux-intensifying machine," *IEEE Trans. Ind. Appl.*, vol. 51, no. 4, pp. 2984-2989, Jul./Aug. 2015.

[21] M. Ibrahim, L. Masisi, and P. Pillay, "Design of variable flux permanent magnet machine for reduced inverter rating," *IEEE Trans. Ind. Appl.*, vol. 51, no. 5, pp. 3666–3674, Sep./Oct. 2015.

[22] M. Ibrahim, L. Masisi, and P. Pillay, "Design of variable-flux permanent magnet machines using Alnico magnets," *IEEE Trans. Ind. Appl.*, vol. 51, no. 6, pp. 4482–4491, Nov./Dec. 2015.

[23] A. Takbash and P. Pillay, "Design optimization of a new spoke type variable-flux motor using AlNiCo permanent-magnet," in *Proc. Electric Machines and Drives Conference (IEMDC 2017)*, Miami, FL, IEEE, May, 2017.

[24] R. Thike and P. Pillay, "Characterization of a variable flux machine for transportation using a vector controlled drive," *IEEE Trans. Transport. Electrific.*, 2018, accepted.

[25] A. M. Ajehaimi, P. Pillay, "Operating envelopes of the variable flux machine with positive reluctance torque," *IEEE Trans. Transport. Electrific.*, 2018, in press.

[26] Y. Zhou, Y. Chen, J. Shen, "Analysis and improvement of a hybrid permanent-magnet memory motor," *IEEE Trans. Energy Concers.*, vol. 31, no. 3, pp. 915-923, Sept. 2016.

[27] J. Chen, J. Li, and R. Qu, "Maximum-torque-per-ampere and magnetization-state control of a variable-flux permanent magnet machine," *IEEE Trans. Ind. Electron.*, vol. 65, no. 2, pp. 1158-1169, Feb. 2018.

[28] A. M. Akrem and P. Pillay, "Novel flux linkage estimation algorithm for a variable flux PMSM," *IEEE Trans. Ind. Appl.*, 2018, in press.

[29] A. Athavale, D. J. Erato, and R. Lorenz, "Enabling driving cycle loss reduction in variable flux PMSMs via closed-loop magnetization state control," *IEEE Trans. Ind. Appl.*, 2018, in press.

[30] A. Athavale, K. Sasaki, T. Kato, and R. Lorenz, "Magnetization state estimation in variable-flux PMSMs," in *Proc. Int. Electr. Mach. Drives Conf. (IEMDC 2017)*, Miami, FL, 2017, pp. 1-8.

[31] B. S. Gagas, K. Sasaki, A. Athavale, T. Kato, R. D. Lorenz, "Magnet temperature effects on the useful properties of variable flux pm synchronous machines and a mitigating method for magnetization changes," *IEEE Trans. Ind. Appl.*, vol. 53, no. 3, pp. 2189-2199, May/Jun. 2017.

[32] Y. Gong, K. T. Chau, J. Z. Jiang, C. Yu, and W. Li, "Analysis of doubly salient memory motors using preisach theory," *IEEE Trans. Magn.*, vol. 45, no. 10, pp. 4676–4679, Oct. 2009.

[33] C. Yu and K. T. Chau, "Design, analysis, and control of DC-excited memory motors," *IEEE Trans. Energy Convers.*, vol. 26, no. 2, pp. 479-489, Jun. 2011.

[34] X. Zhu, L. Quan, D. Chen, M. Cheng, W. Hua, and X. Sun, "Electromagnetic performance analysis of a new stator-permanent-magnet doubly salient flux memory motor using a piecewise-linear hysteresis model," *IEEE Trans. Magn.*, vol. 47, no. 5, pp. 1106-1109 , May 2011.

[35] C. Yu, S. Niu, S. L. Ho, W. Fu, and L. Li, "Hysteresis modeling in transient analysis of electric motors with AlNiCo magnets," *IEEE Trans. Magn.*, vol. 51, no. 3, Art. No. 7300804, Mar. 2015.

[36] C. Yu and K. T. Chau, "Dual-mode operation of DC-excited memory motors under flux regulation," *IEEE Trans. Ind. Appl.*, vol. 47, no. 5, pp. 2031-2041, Sep./Oct. 2011.

[37] F. Li, K. T. Chau, C. Liu, and Z. Zhang, "Design principles of permanent magnet dual-memory machines," *IEEE Trans. Magn.*, vol. 48, no. 11, pp. 3234-3237, Nov. 2012.

[38] X. Zhu, Z. Xiang, L. Quan, W. Wu, and Y. Du, "Multimode optimization design methodology for a flux-controllable stator permanent magnet memory motor considering driving cycles," *IEEE Trans. Ind. Electron.*, vol. 65, no. 7, pp. 5353-5366, Jul. 2018.

[39] Q. Wang, S. Niu, S. L. Ho, W. Fu, and S. Zuo, "Design and analysis of novel magnetic flux-modulated mnemonic machines," *IET. Electr. Appl.*, vol. 51, no. 3, Art. No. 7300804, Mar. 2015.

[40] H. Yang, Z. Q. Zhu, H. Lin, and S. Lyu, "Comparative study of hybrid PM memory machines having single- and dual-stator configurations," *IEEE Trans. Ind. Electron.*, 2018, in press.

[41] H. Yang, H. Lin, Z. Q. Zhu, D. Wang, S. Fang, and Y. Huang, "A variable-flux hybrid-PM switched-flux memory machine for EV/HEV applications*," IEEE Trans. Ind. Appl.*, vol. 52, no. 3, pp. 2203-2214, May/Jun. 2014.

[42] H. Yang, H. Lin, Z. Q. Zhu, E. Zhuang, S. Fang, Y. Huang, "Operating-envelop-expandable control strategy for switched flux hybrid magnet memory machine," in *Proc. Energy Convers. Congr. and Expo. (ECCE), 2016 IEEE*, Milwaukee, U.S., 2016, pp. 1-8.

[43] G. Yang, M. Lin, N. Li, X. Fu and K. Liu, "Maximum torque output control of hybrid permanent magnet axial field flux-switching memory machine," *2017 IEEE Energy Conversion Congress and Exposition (ECCE)*, Cincinnati, OH, 2017, pp. 1212-1219.